Springer

KSME

Journal of Mechanical Science and Technology 27 (11) (2013) 3253~3265
www.springerlink.com/content/1738-494x
DOI 10.1007/s12206-013-0848-6

A mathematical model for the prediction of the injected mass diagram of a S.I. engine gas injector †

Marco Cammalleri, Emiliano Pipitone*, Stefano Beccari and Giuseppe Genchi

University of Palermo,Viale delle Scienze, 90128 Palermo, Italy

(Manuscript Received January 4, 2013; Revised April 19, 2013; Accepted June 11, 2013)

Abstract

A mathematical model of gaseous fuel solenoid injector for spark ignition engine has been realized and validated through experimental data. The gas injector was studied with particular reference to the complex needle motion during the opening and closing phases, which strongly affects the amount of fuel injected. As is known, in fact, when the injector nozzle is widely open, the mass flow depends only on the fluid pressure and temperature upstream the injector: this allows one to control the injected fuel mass acting on the "injection time" (the period during which the injector solenoid is energized). This makes the correlation between the injected fuel mass and the injection time linear, except for the lower injection times, where we experimentally observed strong nonlinearities. These nonlinearities arise by the injector outflow area variation caused by the needle bounces due to impacts during the opening and closing transients [1] and may seriously compromise the mixture quality control, thus increasing both fuel consumption and pollutant emissions, above all because the S.I. catalytic conversion system has a very low efficiency for non-stoichiometric mixtures. Moreover, in recent works [2, 3] we tested the simultaneous combustion of a gaseous fuel (compressed natural gas, CNG, or liquefied petroleum gas, LPG) and gasoline in a spark ignition engine obtaining great improvement both in engine efficiency and pollutant emissions with respect to pure gasoline operation mode; this third operating mode of bi-fuel engines, called "double fuel" combustion, requires small amounts of gaseous fuel, hence forcing the injectors to work in the non-monotonic zone of the injected mass diagram, where the control on air-fuel ratio is poor. Starting from these considerations we investigated the fuel injector dynamics with the aim to improve its performance in the low injection times range. The first part of this paper deals with the realization of a mathematical model for the prediction of both the needle motion and the injected mass for choked flow condition, while the second part presents the model calibration and validation, performed by means of experimental data obtained on the engine test bed of the internal combustion engine laboratory of the University of Palermo.

Keywords: CNG; Gas injector; Injector model; Spark ignition engine

1. Introduction

A typical gaseous fuel multi-point injection system of modern S.I. engines is composed of the following main elements (see Fig. 1): the gas tank (11), the pressure regulator and the filter (5 and 6), and the fuel rail (12) which feeds each injector (8). In the setup of Fig. 1 the fuel is injected into the inlet duct (port injection). The regulator reduces the gas pressure from the high level in the tank (10 bar for LPG while CNG is stored at around 200 bar) to the low level in the fuel rail (about 10 bar for CNG and 2 bar for LPG).

The regulator is usually warmed by the engine coolant to avoid freezing due to gas expansion. In some cases the regulator senses the manifold absolute pressure (MAP) to keep a constant pressure difference between the fuel rail and the air manifold. In chocked flow condition, which is the standard operating mode, the gas flow depends only on pressure and temperature upstream the injector and this makes the injected mass directly proportional to the injector opening duration. The electronic control unit (ECU) hence adjusts the injected fuel mass, and then the air-fuel ratio, acting on the "injection time" (i.e., the period during which the injector solenoid is energized), whose value, function of engine speed and load (usually represented by MAP), is stored in memory by means of proper tables. A more precise control of the air-fuel ratio is then performed by means of a closed-loop control using as feedback the lambda sensor output signal.

Fig. 2 shows, in the upper part, a cutaway of the solenoid fuel injector [4] used in the experimental tests and, in the lower part, the electrical circuit used to energize the injector solenoid; the circuit is composed by the power supply, the injector solenoid and the power transistor activated by the ECU.

The injector is mainly composed of a mechanical part, the needle, and an electric part, the solenoid, and these two parts interact, influencing each other through the electromagnetic

*Corresponding author. Tel.: +39 09123897280, Fax.: +39 09123860672
E-mail address: emiliano.pipitone@unipa.it
† Recommended by Editor Yeon June Kang

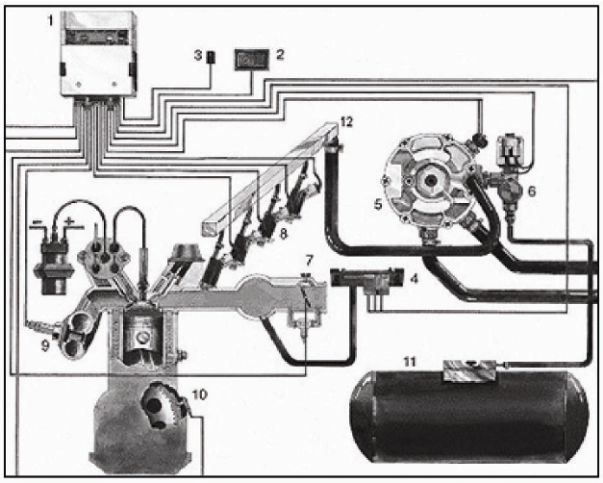

Fig. 1. Gaseous fuel multi point injection setup (1 ECU, 4 MAP sensor, 5 pressure regulator, 6 filter valve, 7 throttle valve, 8 injectors, 9 lambda sensor, 11 gas tank, 12 fuel rail).

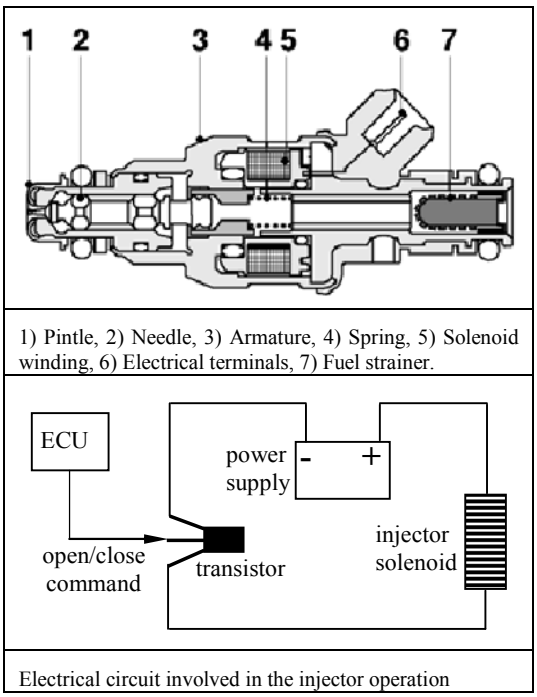

Fig. 2. Cutaway of the fuel injector used in the test (top) and scheme of the injection electrical circuit (bottom).

field. The needle movement in fact influences the solenoid current which, in turn, acts on the needle by the electromagnetic force.

When the solenoid is not energized (i.e., the electrical circuit is open) the needle is kept in closed position by both the fuel pressure and the spring load. When the ECU activates the transistor (which can be considered a "digital switch"), this closes the electrical circuit and the current rises in the solenoid windings, according to the R-L circuit law (see the lower part

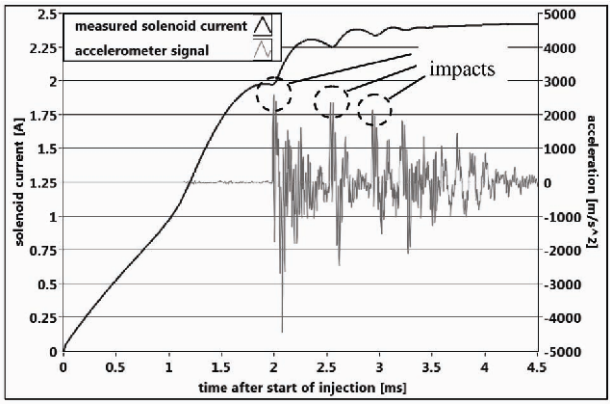

Fig. 3. Solenoid current and armature accelerations during injector opening phase.

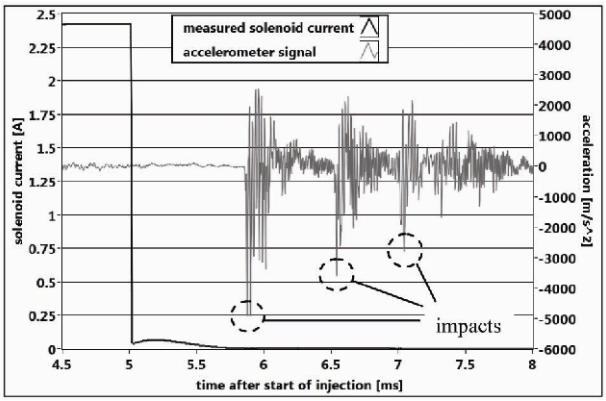

Fig. 4. Solenoid current and armature accelerations during injector closing phase.

of Fig. 2); the needle then is thrust by the electromagnetic force and moves from the closed towards the open position, thus knocking against the stop surface at the end of the lift. If this impact is strong enough, the needle may bounce and move towards the closed position, where another impact may occur. If the injection time is long enough, at the end of the repeated bounces, the needle, under the effect of the electromagnetic field, will remain in open position. Once finished the injection time, the ECU deactivates the transistor which opens the circuit producing an instantaneous drop of the solenoid current; the needle is forced to return to the closed position by the fuel pressure and the spring load, thus knocking against the closed position seat. All the impacts on the two stop surfaces produce needle bounces, which, in turn, due to the reciprocal interaction between needle and coil-winding, influences the solenoid current [1]: Figs. 3 and 4 show the solenoid current together with the output signal from an accelerometer mounted on the armature of an injector used for test, during the injector opening and closing phases.

As shown, the needle opening and closing impacts appear as cusps on the solenoid current and as prominent spikes on the accelerometer output signal. In particular, Fig. 3 shows

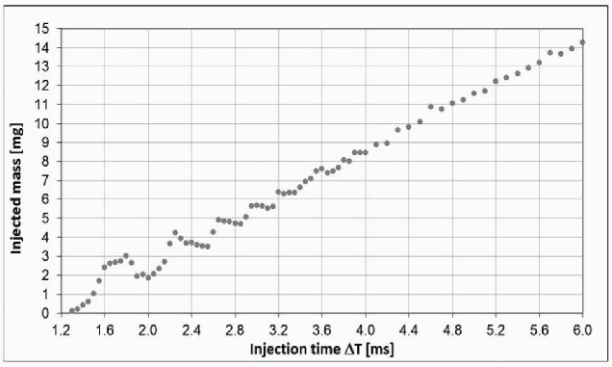

Fig. 5. Injector flow chart: measured injected mass for different injection duration Δt (injector operated with air at 9 bar).

that for the tested injector fed with air at 9 bar, the opening phase bounces go on for about 4 ms, after start of injection, while in the closing phase their duration is shorter, i.e., about 3 ms after stop of injection. The importance of these bounces relies on the great variations they produce on the injected mass, since the instantaneous flow section depends on the needle position; assuming a linear correlation between flow section area and needle position, it results that during the transient opening or closing phases, the injected mass depends on the integral of the needle position. When the injection time is below the opening phase transient duration (≈4 ms for the injector tested), the needle transient not only is not completed, but is also influenced by the duration of the injection itself. The impact energy of the needle on the opening stop surface, in fact, depends on its kinetic energy, which is related to the duration of the electromagnetic force applied, and hence to the injection time. It results that, for injection time shorter than 4 ms, changing the injection duration modifies the needle movement and hence the integral of its position, which causes a variation in the injected mass. This introduces a non-linear dependence between the injected mass and the injection time, as is evident in the injector flow chart shown in Fig. 5.

This diagram reports the measured injected mass (details on the experimental setup and method are given further in chapter 3) for each of the injection times imposed on the injector fed with air at 9 bar absolute pressure. It is worth to remark that this diagram does not represent the integral of the gas mass flow as function of time, but rather the measured injected mass for each single injection, whose duration is the injection time Δt. As can be noted, the needle bounces have a considerable influence on the total injected mass for injection duration shorter than the bounces duration (≈ 4 ms). The non-monotonic behavior arises from the flow section variations caused by the needle bounces, whose intensities, as already pointed out, are related to the needle kinetic energy, which depends on the duration of the electromagnetic force applied: it may happen then that the stronger impact of the needle on the opening seat, obtained by increasing the injection time, causes a faster return of the needle towards the closed position, and hence a faster decrease of the injector outflow section, which implies a decrease on the injected mass. This conclusion, confirmed by means of oscilloscope observation of the solenoid current and armature acceleration waveforms together with mass flow data acquisition carried out for 9 bar air injection with injection duration between 1.8 and 2.5 ms, explains the parts of the injector flow chart which exhibits negative derivatives. A further increase of the injection time implies a return toward the open position of the needle, hence an increase in the injector flow section and, as a consequence, an increase in the injected mass.

When the injection time is long enough to let the needle complete all the opening bounces (≥ 4 ms), all the opening and closing transient phenomena identically repeat at each single injection, and hence their effects no longer influence the total injected mass, which becomes then a linear function of the injection time.

The nonlinearities of the injected mass diagram can cause inaccurate control over the air-fuel ratio; this, in turn, can lead to both higher fuel consumption and higher pollutant emissions because of the catalytic converter's lower efficiency due to the non-stoichiometric air-fuel mixture.

However, these nonlinearities have not been observed using gasoline; hence this study focuses on the injector dynamics modeling when using gaseous fuels.

Moreover, in recent experimental works [2, 3], the authors tested the simultaneous combustion of a gaseous fuel (compressed natural gas or LPG) and gasoline in a spark ignition engine, obtaining great improvement both in engine efficiency and pollutant emissions with respect to pure gasoline operation mode; the addition of CNG (or LPG) to the gasoline-air mixtures strongly improved the knocking resistance, thus allowing the engine to run at full load with a global stoichiometric mixture and with optimal combustion phase (spark advance). This third operating mode of bi-fuel engines, called "*double fuel*" combustion, requires small amounts of gaseous fuel, hence forcing the injectors to work in the non-monotonic zone of the injected mass diagram, where the control on air-fuel ratio is poor. The authors hence decided to study and model the complex needle motion during the opening and closing phases so as to predict the amount of fuel injected for each injection time; the model realized has been calibrated and validated by means of experimental data collected on the test bench. Once calibrated, such a model can be effectively used to study and test injection strategies with the aim to "linearize" as much as possible the injected mass diagram, thus improving air-fuel ratio control in the lower injection times zone.

There is considerable literature on fuel injector modeling: some authors explored the details of fuel spray formation and mixture with air [5], while others studied the control strategies for the optimization of the injection system operation [1, 6, 7]; the presence of a non-monotonic zone in the injector flow chart, however, has never been studied in detail, least of all its correlation with the needle motion.

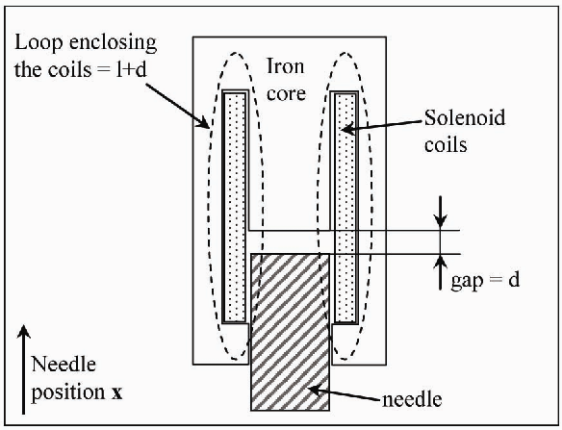

Fig. 6. Magnetic circuit model.

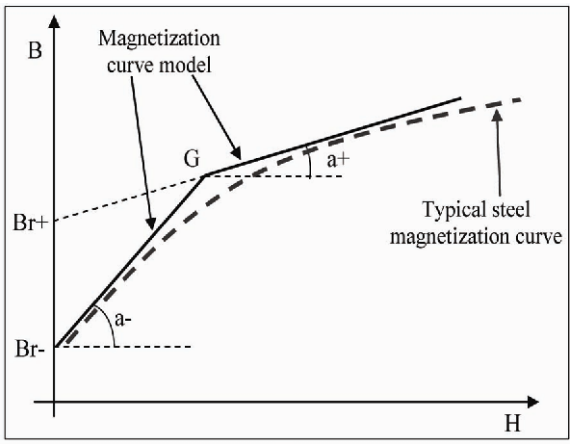

Fig. 7. Steel magnetization curve model.

2. Mathematical model

2.1 Electromagnetic circuit

A fuel injector behaves just like an electromagnet [1, 6]: in fact, when the current i flows through the solenoid coils a magnetic induction B appears in the steel core (see Fig. 6); this magnetic induction B is related to the magnetic field H through the equation: $B = \mu_0 \mu_r H$, being μ_0 the space permeability and μ_r the steel relative permeability. The steel magnetization curve (represented by a bold dashed curve in Fig. 7) has been modelled by two line segments, as shown in Fig. 7, whose slope and intercept (residual magnetization) are a and B_r respectively; the superscripts $(\ldots)^-$ and $(\ldots)^+$ refer to the values before and after the steel magnetic permeability change, which is represented by the intersection point G.

The loop that encloses the coils in Fig. 6 has a constant total length equal to $l+d$, where l is the path length inside the steel and d the path length in the gap. Ampere's law, applied to the above mentioned loop, states that:

$$\oint H \cdot d\sigma = N \cdot i \quad \Rightarrow \quad H_1 \cdot l + H_0 \cdot d = N \cdot i \tag{1}$$

where σ is the path along the loop, i the coil current, N the number of coils enclosed by the loop, H_0 the magnetic field in the air and H_1 in the steel. The magnetic flux ϕ_B enclosed by the coils is:

$$\phi_B = N \cdot A \cdot B$$

where A is the solenoid cross-section area. Since the enclosed magnetic flux must remain constant, the magnetic induction B inside the steel must be equal to the one outside (i.e., $B = B_0$) then:

$$H_0 = \frac{B_0}{\mu_0} = \frac{B}{\mu_0} = \frac{B_r + a \cdot H_1}{\mu_0}.$$

Thus Eq. (1) gives:

$$B(i) = \frac{B_r \cdot \mu_0 \cdot l + a \cdot \mu_0 \cdot N \cdot i}{\mu_0 \cdot l + a \cdot d}. \tag{2}$$

Since the loop length $(l + d)$ is constant, the l and d time derivatives are:

$$\dot{l} = -\dot{d} = \dot{x}$$

where x is the needle position ($x = 0$ when the needle is in closed position, as in Fig. 6).

The time derivative of ϕ_B is:

$$\dot{\phi}_B = \frac{d\phi_B}{dt} = L\frac{di}{dt} + \left[L\frac{B_r}{N \cdot a} \cdot \frac{a \cdot (d+l)}{\mu_0 \cdot l + a \cdot d} \right] \dot{x} + \left[L\frac{a - \mu_0}{\mu_0 \cdot l + a \cdot d} \right] i \cdot \dot{x} \tag{3}$$

being L the circuit inductance:

$$L = \frac{A \cdot N^2}{\left(\frac{l}{a}\right) + \left(\frac{d}{\mu_0}\right)}. \tag{4}$$

2.2 The electromagnetic force

The magnetic energy per unit volume in the gap is:

$$\int_0^H H \cdot dB = \frac{B_0^2}{2\mu_0}.$$

For a given virtual displacement dx of the needle, equating the electromagnetic force (F_{em}) work with the energy variation in the gap gives:

$$F_{em} \cdot dx = \frac{B_0^2}{2\mu_0} A \cdot dx \quad \Rightarrow \quad F_{em} = \frac{A \cdot B_0^2}{2\mu_0} = \frac{A \cdot B^2}{2\mu_0}. \tag{5}$$

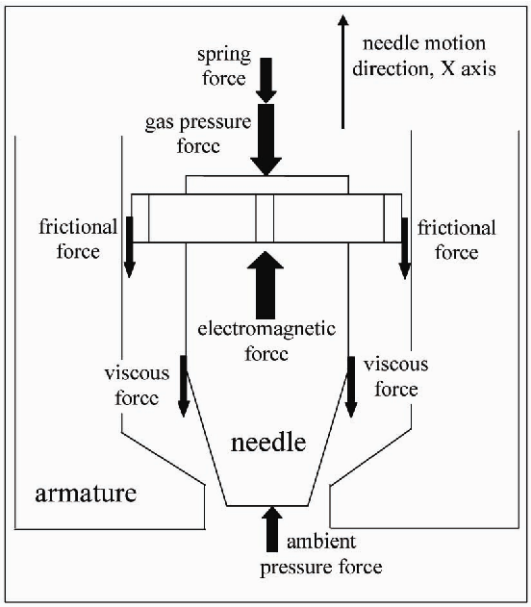

Fig. 8. Injector needle free body diagram.

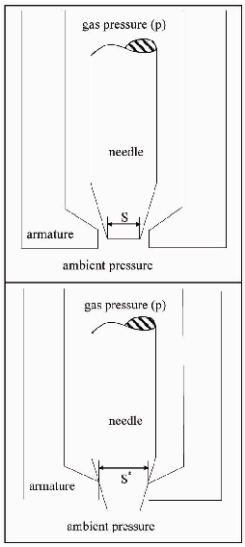

Fig. 9. Schematic representation of the injector outlet: in the upper picture the needle is in open position, while in the lower picture it is in closed position.

Considering Eqs. (2) and (5), the electromagnetic force can be written as:

$$F_{em} = (c_1 + c_2 i)^2 \tag{6}$$

being:

$$c_1 = \frac{\sqrt{\frac{A}{2\mu_0}} \cdot \frac{B_r \cdot l}{a}}{\left(\frac{l}{a} + \frac{d}{\mu_0}\right)} \qquad c_2 = \frac{\sqrt{\frac{A}{2\mu_0}} \cdot N}{\left(\frac{l}{a} + \frac{d}{\mu_0}\right)}. \tag{7}$$

As already mentioned, the loop length (l + d) is constant, which implies that:

$$\frac{dL}{dx} \approx 0, \quad \frac{dc_1}{dx} \approx 0, \quad \frac{dc_2}{dx} \approx 0.$$

Hence the parameters L, c_1 and c_2 can be assumed constant with respect to the needle position.

2.3 Dynamic equilibrium equation

As shown in the free body diagram of Fig. 8, the forces acting on the injector needle with the direction of the needle motion are:

(1) The spring force, equal to $k \cdot (x+\delta)$, where δ is the spring preload deformation and k is the spring constant.

(2) The electromagnetic force F_{em}.

(3) The gas force F_{gas}, which tends to put the needle in closed position and whose expression depends on whether the injector is open or not.

(4) The Coulomb frictional force between needle and guides F_{fr} and the viscous force F_v due to the gas, both of which counteract the needle movements.

When the injector is open (i.e., the needle is not in closed position, as represented in the upper picture of Fig. 9), the flow can be assumed to be almost equal to a gas expansion through a convergent nozzle, where the gas pressure decreases from the stagnation value p to the ambient value p_{amb}. The gas force resultant F_{gas} in the direction of the needle motion should then depend on the integral of the gas pressure extended to the whole needle surface, and is here substituted by the term $(p \cdot S_{eq} - p_{amb} \cdot S)$, where S_{eq} is an "equivalent" area defined so that the product $(p \cdot S_{eq})$ represents the closing force exerted by gas on the needle when it is not in closed position; the term S instead indicates the needle area subject to the ambient pressure p_{amb}.

When the injector lies in closed position, as shown in the lower picture of Fig. 9, both gas pressure p and ambient pressure p_{amb} act on surfaces whose whole extension is S^*; hence the gas force resultant in the direction of the needle motion is $(p - p_{amb}) \cdot S^*$.

The viscous force is proportional to the needle speed so it can be written as: $F_v = -c \cdot \dot{x}$ where the viscous damping coefficient c must be determined.

When the needle is not in contact with the seat surfaces, its equilibrium equation can be written as follows:

$$M\ddot{x} + c\dot{x} + kx = F_{em} - k\delta - F_{fr} sign(\dot{x}) - (pS_{eq} - p_{amb}S) \tag{8}$$

being M the needle mass.

Defining the following dimensionless parameters:

$$X = \frac{x}{x_{\max}} \qquad I = \frac{i}{V/R} \qquad I_g = \frac{i_g}{V/R}$$
$$d\vartheta = \omega_n \cdot dt \qquad \omega_n = \sqrt{\frac{k}{M}} \qquad X' = \frac{dX}{d\vartheta} \quad . \tag{9}$$
$$X'' = \frac{dX'}{d\vartheta} \qquad I' = \frac{dI}{d\vartheta}$$

Hence

$$\dot{x} = \frac{dx}{dt} = x_{\max}\frac{dX}{d\vartheta}\frac{d\vartheta}{dt} = x_{\max} \cdot X' \cdot \omega_n$$

where x_{max} represents the needle lift, i_g the solenoid current corresponding to the point G of Fig. 7, V the supply voltage, R the solenoid electric resistance, t the time and ω_n the natural circular frequency of the spring-needle system; Eq. (8) then becomes:

$$X'' + 2\zeta \cdot X' + X = \left(\gamma_1 + \gamma_2 \cdot I\right)^2 - P \cdot \gamma_3 - \gamma_4 \cdot sign\left(X'\right) + \gamma_5 \tag{10}$$

where $\zeta = \frac{c \cdot \omega_n}{2k}$ is the viscous damping factor, $P = \frac{p}{p_{amb}}$ is the dimensionless gas pressure and

$$\gamma_1 = \frac{c_1}{\sqrt{k \cdot x_{\max}}} \quad \gamma_2 = \frac{c_2 \dfrac{V}{R}}{\sqrt{k \cdot x_{\max}}} \quad \gamma_3 = \frac{p_{amb} \cdot S_{eq}}{k \cdot x_{\max}}$$
$$\gamma_4 = \frac{F_{fr}}{k \cdot x_{\max}} \quad \gamma_5 = \frac{p_{amb} \cdot S - k \cdot \delta}{k \cdot x_{\max}} . \tag{11}$$

Eq. (10), as already mentioned, applies whenever the needle is not in contact with seat surfaces.

2.4 Impact modeling

To take into account the needle impacts on the seat surfaces, the following equations have been introduced in the model to evaluate, in place of Eq. (10), the needle speed variations across each impact:

$$X'_{ai} = -\sqrt{\xi} \cdot X'_{bi} \tag{12}$$

where X'_{bi} and X'_{ai} are the dimensionless needle velocities before and after impact, respectively, and ξ is the coefficient of restitution (the ratio between the kinetic energy after and before the impact).

2.5 Electro-magnetic circuit equation

The solenoid current i depends on the supply voltage V and on the induced voltage caused by the magnetic flux ϕ_B variation. Ohm's law, together with the Faraday-Lenz law, brings:

$$R\,i = V - \frac{d\phi_B}{dt} \quad .$$

By introducing the dimensionless variables reported in Eq. (9), Eq. (3) becomes:

$$I' = \frac{1 - I - \left(\lambda_1 + \lambda_2 \cdot I\right) \cdot X'}{\Theta} \quad . \tag{13}$$

The parameters Θ, λ_1 and λ_2 are defined as follows:

$$\Theta = \frac{L}{R}\omega_n = \text{dimensionless time constant}$$
$$\lambda_1 = \frac{B_r}{\mu_0 \cdot N + a \cdot N \cdot \dfrac{d}{l}} \cdot \frac{L}{V} \cdot \omega_n \cdot x_{\max} \tag{14}$$
$$\lambda_2 = \frac{\dfrac{1}{\mu_0} - \dfrac{1}{a}}{\dfrac{1}{a} + \dfrac{d}{\mu_0}} \cdot \Theta \cdot x_{\max} .$$

2.6 Injected mass calculation

The flow through the gas injector can be assumed to be equivalent to the flow through a convergent nozzle. Considering the injector to be in chocked flow conditions (supposing that, as usual, the ratio between fuel rail pressure and manifold pressure is ≥ 2), for a fixed needle position; hence, assuming the gas to be a perfect gas, the steady mass flow is $\dot{m}$ proportional to the upstream pressure and to the effective outflow area A_{out} (the theoretical area $A_{out,th}$ corrected by the discharge coefficient ε):

$$\dot{m} = A_{out,th} \cdot \varepsilon \cdot \frac{p}{\sqrt{R'T}} \cdot \sqrt{\nu \cdot \left(\frac{2}{\nu+1}\right)^{\frac{\nu+1}{\nu-1}}} =$$
$$= A_{out} \cdot \frac{p}{\sqrt{R'T}} \cdot f\left(\nu\right) \tag{15}$$

being T the gas temperature, R' the gas constant and ν the gas isentropic coefficient (the ratio between gas constant pressure and constant volume specific heat = c_P/c_V).

The mean mass flows measured with full open injector under different feeding pressure p (and constant temperature T) confirmed this proportionality.

For the evaluation of the total injected mass during transient phenomena, however, the variation of the discharge coefficient as a function of the needle position should be known. However, to preserve model simplicity, we decided to assume a constant value for the discharge coefficient. In this way, the

instantaneous effective outflow area A_{out} results to be proportional to the needle position X and can be evaluated as follows:

$$A_{out} = X \cdot A_{FO}$$

where A_{FO} represents the experimentally determined fully open injector effective outflow area.

Hence, from Eq. (15), the injected mass m_{calc} can be calculated as:

$$m_{calc} = \int \dot{m} \cdot dt = \int \dot{m} \cdot \frac{d\vartheta}{\omega_n} = \int X \cdot A_{FO} \cdot \frac{p}{\sqrt{R'T}} \cdot f(\nu) \cdot \frac{d\vartheta}{\omega_n} =$$
$$= A_{FO} \cdot \frac{p}{\sqrt{R'T}} \cdot \frac{f(\nu)}{\omega_n} \int X \cdot d\vartheta . \quad (16)$$

3. Experimental tests and model calibration

The needle motion and the mass injected can be determined hence by solving the model equation set represented by the two differential Eqs. (10) and (13), together with impact Eq. (12) and injected mass Eq. (16). This set of equations constitutes a hybrid dynamic system, since the impact equation introduces a discontinuity on needle speed. The integration has been performed by means of the Euler algorithm (ode1) with a fixed time step of 1/3200 ms; this specific time step has been selected because it allowed us to avoid the numeric chattering typical of hybrid dynamic systems and to obtain a satisfactory matching between numerical and experimental injected mass together with low computational times. Other integration algorithms have been considered, such as Heun (ode2) and Dormand-Prince (ode8) with fixed time step of 1/3200 ms, or Runge-Kutta (ode45) with a maximum time step of 1/400 ms: in all these cases the solution found, in terms of injected mass diagram, was almost identical to the one obtained by the simple Euler method, while the calculation time increased significantly with the order of the solver. In particular, by employing the more sophisticated algorithm (Runge-Kutta, ode45) the computational time increased by 87%.

As shown, the model has been expressed in a dimensionless form and a great effort has been made to reduce as much as possible the number of parameters to determine for calibration, which are now: ζ, γ_1, γ_2, γ_3, γ_4, γ_5, λ_1, λ_2, Θ and ξ.

Since five of these parameters (γ_1, γ_2, λ_1, λ_2 and Θ) change value across the point G in the magnetization curve of Fig. 7, then the number of parameters to determine becomes fifteen. Some considerations described further on, however, allowed a substantial reduction in the amount of parameters to fix.

The model was calibrated and validated by means of experimental data collected using the natural gas BOSCH injector mounted on a FIAT 1242cc bi-fuel engine. The injector was fed with air at different pressures and actuated by means of 0-5 Volts TTL pulses generated by a national instruments counter board PCI 6602 programmed with LabVIEW. As usually done for internal combustion engine injection or ignition management, an IGBT transistor was used to transform the low power digital pulses into the high current square waveforms necessary for injector solenoid excitation (see the lower picture in Fig. 2). A Bruel & Kjaer Cubic DeltaTron 4502 accelerometer was placed on the injector armature to detect needle impacts. A clamp-on ammeter LEM PR20 with a frequency response of 20 kHz was used to acquire the solenoid current, while the air mass flow was measured by means of a Bronkhorst mini CORI-FLOW M13, a Coriolis-type mass flow meter which features a measuring range of 100-2000 g/h with an accuracy of ± 0.2% of the read value. The injector was activated with frequencies ranging from 10 to 70 Hz so as to obtain mass flows in the measurable range; for each injection time, the experimental injected mass m_{exp} was then derived from the measured mass flow and injection frequency f_{inj}:

$$m_{\exp} = \frac{\dot{m}}{f_{inj}} .$$

All the necessary quantities were acquired by means of a national instruments DAQ board PCI-6133, employing a sample frequency of 400 kHz and using the generated TTL pulse as trigger for data acquisition. For each injection time, the complete waveforms of input voltage, solenoid current and accelerometer output were recorded for 100 consecutive injections, while mass flow, gas pressure and temperature were recorded as mean values over the 100 injection. In this way, for each injection pressure tested, it was possible to obtain a complete injector chart (as, for example, shown in Fig. 5) reporting the total injected gas mass for each injection time between 1.00 and 6.00 ms, with an increment of 0.05 ms.

3.1 Model calibration

A fundamental parameter for model calibration is represented by the maximum current i_0 for which the needle remains in closed position and the corresponding Δt_0 (the time delay from the start of injection pulse to needle movement): in this condition the resultant of thrust exerted by both the spring and the gas pressure is exactly counterbalanced by the electromagnetic force; for higher currents, hence, the electromagnetic force determines the needle movement. Obviously, both the solenoid current i_0 and the delay Δt_0 depend on the gas pressure p.

As already mentioned, when the needle is in closed position (the lower picture of Fig. 9), the force due to the gas pressure can be expressed as $S^* (p-p_{amb})$, and hence Eq. (8) can be written as follows:

$$F_{em}(i_0) = F_{em0} = k \cdot \delta + F_{fr} + S^* \cdot (p - p_{amb})$$

Table 1. Coefficients obtained by interpolation.

$\frac{k\cdot\delta+F_{fr}}{\left(c_2^-\right)^2}$ [A^2]	$\frac{S^*}{\left(c_2^-\right)^2}$ [A^2/bar]	$\frac{c_1^-}{c_2^-}$ [A]
0.114	0.119	0.00

and Eq. (6) becomes:

$$F_{em0}=\left(c_1+c_2\cdot i_0\right)^2 .$$

Then the correlation between gas pressure and current i_0 can be written as follows:

$$i_0=\sqrt{\frac{k\cdot\delta+F_{fr}}{\left(c_2\right)^2}+\frac{S^*}{\left(c_2\right)^2}\cdot\left(p-p_{amb}\right)}-\frac{c_1}{c_2} \tag{17}$$

$$if\ i_0<i_g\ (i.e.\ p\le 8bar)\Rightarrow c_1=c_1^-\ ;\quad c_2=c_2^-$$
$$if\ i_0>i_g\ (i.e.\ p>8bar)\Rightarrow c_1=c_1^+\ ;\quad c_2=c_2^+$$

where superscripts $(...)^-$ and $(...)^+$ refer to the values before and after the steel magnetic permeability change.

When the needle starts to move, the injector armature accelerates in the opposite direction, thus causing a waveform in the accelerometer output signal, whose analysis allowed a sufficiently precise determination of both current i_0 and delay Δt_0.

Several tests were performed to determine the current i_0 for different gas pressures (see Fig. 10); the experimental data were interpolated by means of Eq. (17) for gas pressure up to 8 bar to determine the coefficients reported in Table 1.

It was not possible to trace a similar correlation for gas pressures higher than 8 bar (i.e., for current i_0 higher than i_g) because, for the fixed voltage supply of 13 Volts, the electromagnetic force generated by the solenoid was not able to move the needle from the closed position for gas pressure above 11 bar; this limited the amount of experimental data available (only three points in Fig. 10 for gas pressure higher than 8 bar), thus preventing to trace a reliable correlation with the current i_0. Hence a local linear interpolation between each couple of available experimental points was introduced in the model to evaluate the current i_0 for each pressure between 8 and 11 bar.

As can be observed in Table 1 the coefficient c_1^- resulted null, which implies that $B_r^- = 0$ and so:

$$\lambda_1^-=\gamma_1^-=\lambda_2^+=0 \qquad \text{and} \qquad \frac{\gamma_1^+}{\gamma_2^-}=\left(1-\frac{L^+}{L^-}\right)\cdot I_g \tag{18}$$

according to Eqs. (7), (11) and (14).

As a consequence of the simplified magnetization curve model assumed and represented in Fig. 7, it follows that

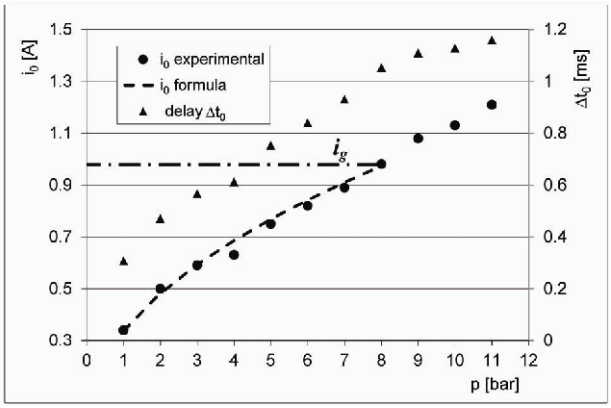

Fig. 10. Needle start moving current i_0 and delay Δt_0 as function of the gas pressure p.

$a^+=\mu_0$, which, from Eq. (14), not only means that $\lambda_2^+=0$, but, together with $B_r^- = 0$, allows also to state that:

$$\frac{\lambda_1^+}{\lambda_2^-}=I_g\cdot\frac{L^+}{L^-} . \tag{19}$$

Moreover, from the definitions given in Eq. (14), it follows that:

$$\frac{\Theta^+}{\Theta^-}=\frac{L^+}{L^-} \tag{20}$$

while, from Eqs. (4) and (7), it can be obtained:

$$\frac{c_2^+}{L^+}=\frac{c_2^-}{L^-}$$

and hence, from Eq. (11):

$$\frac{\gamma_2^+}{\gamma_2^-}=\frac{L^+}{L^-} . \tag{21}$$

The above ratios as well as γ_5 could be obtained by direct measurement of the physical parameters on which they depend. In fact, when the needle is locked, the solenoid behaves as a simple *R-L* circuit: hence, supplying a direct-current voltage to the solenoid, it was possible to determine the parameters i_g, R, L^- and L^+ from the analysis of the electric current flowing into the solenoid.

The needle lift x_{max} together with the surface area S of Eq. (11) was measured by means of high definition camera images taken with injector closed and fully open; the spring constant k and its pre-load deformation δ were instead estimated by means of a laser measurement system together with calibration weights. The values measured for these parameters are

Table 2. Physical parameters determined by direct measurement.

i_g [A]	R [Ohm]	L^- [mH]	L^+ [mH]	x_{max} [mm]	k [N/mm]	δ [mm]	S [mm^2]
1.00	5.40	11.0	2.60	0.300	1.60	0.300	3.00

Table 3. Dimensionless parameters determined by direct measurement.

λ_1^-	γ_1^-	λ_2^+	γ_1^+	λ_1^+	γ_2^+	Θ^+	γ_5
0	0	0	3.34	0.0490	2.48	0.330	-0.375

Table 4. Dimensionless parameters determined by means of the Simplex method.

ζ	γ_2^-	γ_3	γ_4	ξ	Θ^-	λ_2^-
0.0500	10.5	1.30	1.70	0.550	1.40	0.500

Table 5. Physical parameters determined by means of the Simplex method.

c [N/(m/s)]	S_{eq} [mm^2]	F_{fr} [N]	f_n [Hz]	L^-/R [ms]
0.233	6.24	0.816	109	2.04

reported in Table 2.

Eqs. (18)-(21) allow then a substantial reduction of the number of parameters to determine for the model calibration. Table 3 shows the values of the eight dimensionless parameters determined by direct measurements.

The seven remaining parameters to fix (ζ, γ_2^-, γ_3, γ_4, ξ, Θ^-, λ_2^-) were calibrated by means of data fitting using the flow chart experimentally obtained with air at 9 bar absolute pressure (Fig. 5). The injection time was limited to 5 ms because after 4 ms the diagram becomes linear. The experimental data were compared with the model output, defining an error function E as follows:

$$E = \sum_{i=1}^{n} \left| m_{\exp,i} - m_{calc,i} \right| \tag{22}$$

where n is the total number of experimental samples for a single chart, $m_{exp,i}$ is the experimental injected mass corresponding to the i^{th} injection time while $m_{calc,i}$ is the injected mass calculated using Eq. (16).

The minimization of the error function E, performed by means of the Nelder-Mead minimum searching algorithm (or Simplex method [8]), allowed us to evaluate the last seven dimensionless model parameters and the corresponding physical parameters as reported in Tables 4 and 5, respectively.

3.2 Results and discussion

The result of the model identification is shown in Fig. 11, where the injected mass evaluated by the model is compared with the measured: as evident, a very good fit has been reached between experimental data and model prediction (as confirmed by the coefficient $R^2 = 0.998$), since the nonlinearities of the experimental diagram are accurately replicated by the model output. The same diagram also reports the model error (the absolute value of the difference between calculated and measured injected mass) distribution, whose mean and maximum values are 0.16 and 0.60 mg, respectively.

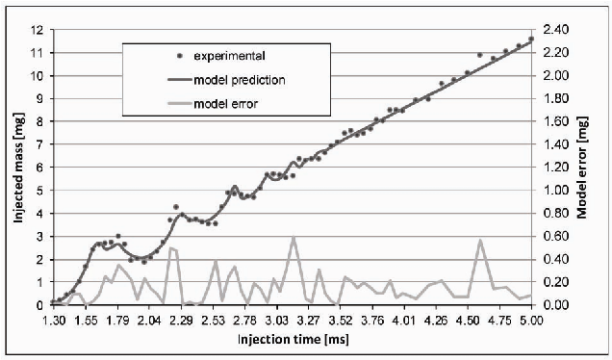

Fig. 11. Injected mass diagram comparison (air pressure 9 bar).

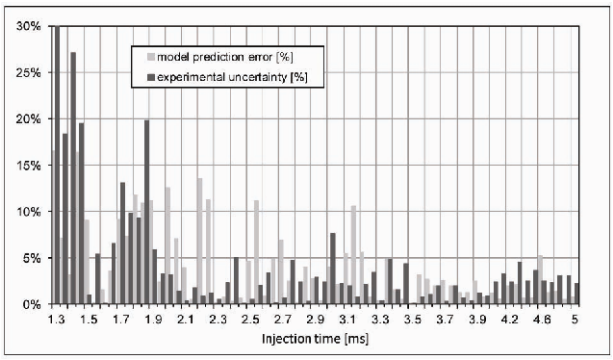

Fig. 12. Model prediction error and experimental uncertainty (air pressure 9 bar).

The graph in the successive Fig. 12 instead reports the model prediction error evaluated as percentage of the measured experimental value, together with the experimental uncertainty, evaluated by means of the standard deviation recorded for each of the 100 mass flow samples acquired during the test.

As is evident, the model evaluation accuracy results to be comparable to the test measurement uncertainties, which, it is worth to mention, are not related to mass flow measurement errors (which, as already mentioned, are less than 1%) but rather to injected mass oscillation around the mean values. The entity of this oscillation has a considerable weight when the injected mass is minimum, while tends to an asymptotic minimum for the higher injected masses. About the same behaviour is exhibited by the model prediction error, even if, as shown in Fig. 11, the absolute error has a more uniform distribution over the whole injection times. In consideration of the distorting effect introduced by the ratio with very low values, in the successive diagrams the model prediction error has been reported only as absolute value.

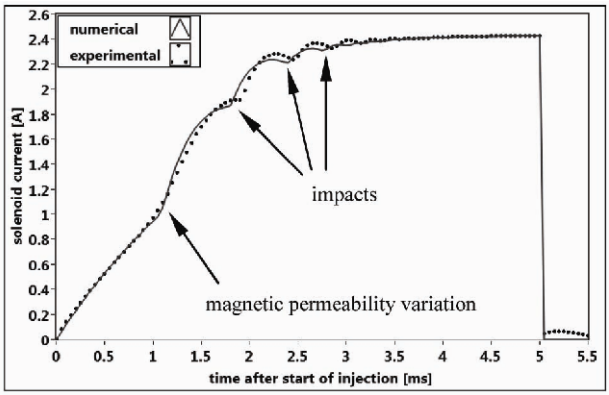

Fig. 13. Solenoid current: model prediction and experimental data (air pressure 9 bar).

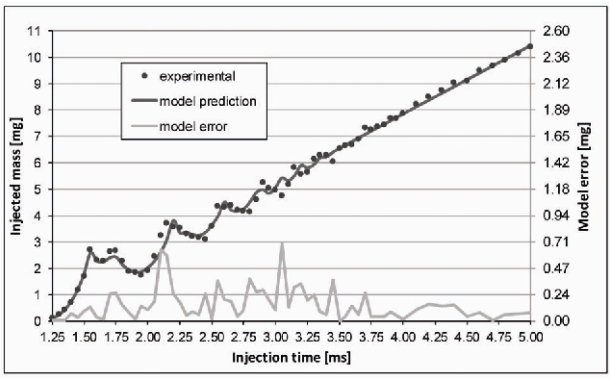

Fig. 14. Injected mass diagram comparison and error distribution (air pressure 8 bar).

A further confirmation of the model predictive capacity was obtained by a comparison between the measured and the evaluated solenoid current in the same condition of air pressure and injection time; as example, the diagram of Fig. 13 shows the good agreement between the measured and the model predicted current during the injector opening phase; as indicated in the diagram, the first cusp is due to variation of the steel magnetic permeability, while the other cusps are connected to the sudden speed change of the needle during the impacts on the seat surfaces.

Once calibrated by means of the experimental data acquired with air at 9 bar, the model was validated by means of two injector flow charts obtained with air pressure of 8 and 10 bar.

The results of the comparison with the injector flow measurements carried out with 8 bar pressure are reported in Fig. 14: the model reproduced again quite well the nonlinearities of the experimental diagram. The very good agreement with the measurements is also confirmed by the regression coefficient $R^2 = 0.997$ obtained. As regards the model prediction error, mean and maximum values of 0.15 and 0.69 mg, respectively, were found, quite similar to that determined for the 9 bar pressure data. A similar conclusion can be drawn for the comparison with the experimental data acquired with air pressure of 10 bar, as shown by the graph in Fig. 15. Also, in this case a

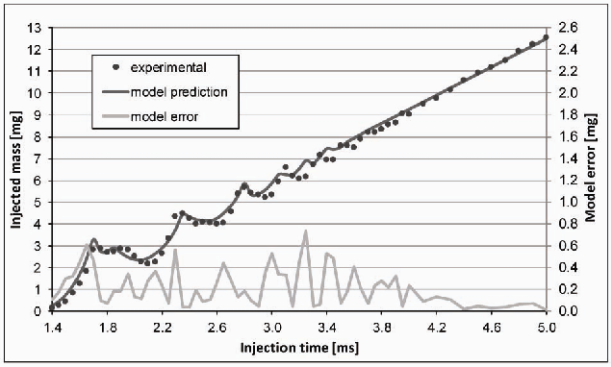

Fig. 15. Injected mass diagram comparison and error distribution (air pressure 10 bar).

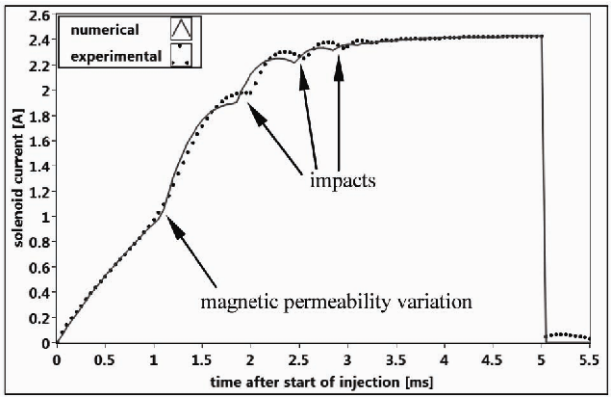

Fig. 16. Solenoid current: model prediction and experimental data (air pressure 8 bar).

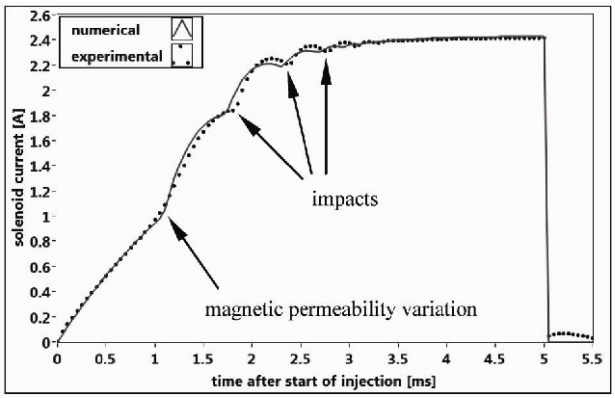

Fig. 17. Solenoid current: model prediction and experimental data (air pressure 10 bar).

good fit was obtained between model prediction and experiments, even if the model constant was calibrated for the 9 bar pressure data. The injected mass evaluation error revealed this time a mean and maximum value of 0.22 and 0.74 mg, respectively, which still represents a good result.

As done using the data collected with air at 9 bar, the solenoid current predicted by the model was compared with the experimental measures also for air pressure of 8 and 10 bar. The comparison, shown in the graphs of Figs. 16 and 17, point

out the reliability of the developed model, whose evaluated current has almost the same progress and cusps positions of the measured current.

To sum up, the mathematical model developed, calibrated by means of experimental data collected with air at 9 bar, has been successfully validated since maintaining a reliable prediction on injected mass and solenoid current also for different air pressure cases.

4. Conclusions

Recent experimental works carried out by the authors on the combustion of gaseous fuels in a spark ignition engine showed the existence of a nonlinear zone in the injected mass diagram of common gas injector. The nonlinearities arise by the injector outflow area variation caused by the needle impacts and bounces during the opening and closing transients and may seriously compromise the mixture quality control, thus increasing both fuel consumption and pollutant emissions.

With the aim of developing advanced injection strategies to linearize as much as possible the injected mass diagram, we decided, as a first step, to study and model the complex dynamics of a solenoid fuel injector: this paper hence deals with the realization of a mathematical model for the prediction of both the needle motion and the injected mass of a gaseous fuel injector, with particular reference to the nonlinearities of the injector flow chart. The model has been realized with a zero-dimensional approach and supposing the injector to work in choked flow condition (which is usual for gaseous fuel injector). Moreover, to lower as much as possible the number of parameters to fix by model identification, a strong grouping work has been done, introducing some dimensionless groups. This allowed us to reduce to only seven the constants to fix by calibration, which was performed by comparing the model output results with experimental data acquired on the test bench. Although a simple zero-dimensional approach has been followed, the model revealed good reliability since not only reproduced quite well the nonlinearities of the real injector flow chart, but proved to predict with unexpected accuracy also the injected mass and the solenoid current related to air pressure cases different from the calibration set. The model prediction error, in terms of injected mass, was found to be of the same order of magnitude of the experimental uncertainties.

Even if more complex phenomena have not been taken into account (choked flow condition inside the injector, gas flow transient phenomena and their interaction with the mechanical needle transient, etc.) the quite good fit obtained with respect to real experimental data led us to believe that all the relevant phenomena have been adequately considered.

The model developed is quite general, and once calibrated by proper experimental data, could be employed for the prediction of the injected mass, regardless of the kind of gas used or of the injection pressure levels.

As a future development, we intend to employ the model to determine proper solenoid current supplying strategies in order to linearize as much as possible the injector mass diagram, thus improving both air-fuel ratio control and pollutant emissions.

Nomenclature

CNG : Compressed natural gas
ECU : Electronic control unit
LPG : Liquefied petroleum gas
MAP : Manifold absolute pressure
S.I. : Spark ignition.
IGBT : Insulated gate bipolar transistor
$\dot{(\ldots)}$: First derivative with respect to time t
$\ddot{(\ldots)}$: Second derivative with respect to time t
$(\ldots)'$: First derivative with respect to dimensionless time ϑ
$(\ldots)''$: Second derivative with respect to dimensionless time ϑ
$(\ldots)^-$: Refers to the values before the steel magnetic permeability change
$(\ldots)^+$: Refers to the values after the steel magnetic permeability change
a : Sslope of the magnetization curve line
A : Solenoid cross-section area
A_{FO} : Fully open injector effective outflow area
A_{out} : Instantaneous injector effective outflow area
$A_{out,th}$: Instantaneous theoretical injector outflow area
B : Magnetic induction in the steel
B_0 : Magnetic induction in the air
B_r : Intercept of the magnetization curve model
c : Viscous damping coefficient of the gas around the needle
c_1, c_2 : Parameters correlating the solenoid current and the electromagnetic force
d : Path length in the air gap
F_{em} : Electromagnetic force
F_{fr} : Frictional force between needle and guides
f_{inj} : Injector activation frequency
f_n : Natural frequency of the spring-needle system
F_v : Viscous force due to the gas
G : Steel magnetic permeability change point
H : Magnetic field
H_0 : Magnetic field in the air
H_1 : Magnetic field in the steel
i : Solenoid electric current
I : Dimensionless solenoid electric current
i_0 : Maximum solenoid current for which the needle remains in closed position
I_0 : Dimensionless current i_0
i_g : Solenoid current corresponding to the steel magnetic permeability change
I_g : Dimensionless current i_g
k : Spring constant
l : Path length inside the steel
L : Circuit inductance

M : Needle mass
$\dot{m}$: Gas mass flow
m_{calc} : Injected mass calculated by the model
$m_{exp.}$: Injected mass experimentally measured
n : Total number of experimental samples for a single injected mass diagram
N : Number of coils in the solenoid
p : Gas (absolute) stagnation pressure
P : Dimensionless gas (absolute) stagnation pressure
p_{amb} : Ambient pressure
R : Solenoid electric resistance
R' : Gas constant
R^2 : R-square coefficient of correlation between experimental data and model prediction
S : Needle area subject to the ambient pressure
S^* : Needle area subject to relative gas pressure (p-p_{amb})
S_{eq} : Needle "equivalent" area subject to gas pressure p
t : Time variable
T : Gas absolute temperature
V : Solenoid supply voltage
x : Needle position
x_{max} : Needle lift
X : Dimensionless needle position
X'_{ai} : Dimensionless needle velocity after impact
X'_{bi} : Dimensionless needle velocity before impact
Δt_0 : Time delay from the start of the injection pulse to needle movement
Δt : Injection time
ϑ : Dimensionless time ($\vartheta = \omega_n t$)
Θ : Dimensionless time constant of the R-L circuit (proportional to ω_n)
δ : Spring preload deformation
ε : Injector discharge coefficient
ϕ_B : Magnetic induction flux enclosed by the coils
ν : Isentropic coefficient (i.e. ratio between gas constant pressure and constant volume specific heat = c_P/c_V)
γ_1, γ_2 : Model dimensionless parameters (see equation 11)
$\gamma_3, \gamma_4, \gamma_5$: Model dimensionless parameters (see equation 11)
λ_1, λ_2 : Model dimensionless parameters (see equation 14)
μ_0 : Space permeability
μ_r : Steel relative permeability
σ : Path along the loop enclosing the coils
ω_n : Natural circular frequency [rad/s] of the spring-needle system
ξ : Impact coefficient of restitution
ζ : Viscous damping factor of the air around the needle

References

[1] D. Dyntar and L. Guzzella, Optimal control for bouncing suppression of CNG injectors, *Journal of Dynamic Systems, Measurement and Control (ASME)*, March, 126 (2004) 47-53.
[2] E. Pipitone and S. Beccari, Performances improvement of a S.I. CNG bi-fuel engine by means of double-fuel injection, *SAE technical paper*, n. 2009-24-0058.
[3] E. Pipitone and S. Beccari, Performances and emissions improvement of an S.I. engine fuelled by LPG/gasoline mixtures, *SAE technical paper*, n. 2010-01-0615.
[4] *Bosch automotive handbook*, Robert Bosch GmbH (1996) ISBN 1-56091-918-3.
[5] M. Baratta, A. E. Catania, E. Spessa, L. Herrmann and K. Roessler, Multi-dimensional modeling of direct natural-gas injection and mixture formation in a stratified-charge SI engine with centrally mounted injector, *SAE International Journal of Engines*, 1 (1) April (2009) 607-626.
[6] S. Di Cairano, A. Bemporad, I. V. Kolmanovsky and D. Hrovat, Model predictive control of magnetically actuated mass spring dampers for automotive applications, *International Journal of Control*, 80 (11) (2007) 1701-1716.
[7] P. Lino, B. Maione, C. Amorese and S. De Matthaeis, Modeling and predictive control of a new injection system for compressed natural gas engines, *Proceedings of the 2006 IEEE International Conference on Control Applications*, Munich, Germany, October 4-6 (2006).
[8] J. A. Nelder and R. Mead, A simplex method for function minimization, *Computer Journal*, 7 (1965) 308-313.

Marco Cammalleri graduated in Mechanical Engineering in 1998 at the University of Palermo. He has been assistant professor since July 2000 and teacher of mechanics of the machines since 2001 at the University of Palermo. Currently he studies about the dynamic of a S.I. engine fuel gas injector, on the rotor dynamics and mechanical vibrations and on design of mechanisms. Previously he carried out theoretical and experimental research on single and split way CVT transmissions and on rubber v-belt mechanics.

Stefano Beccari obtained his Ph.D. in Mechanical Engineering from University of Palermo (Italy) in 2005. He is currently a researcher there in the field of fluid machines. His main research interest is the spark ignition engine performance and efficiency optimization, with particular reference to the bi-fuel engines: gasoline-natural gas and gasoline-LPG.

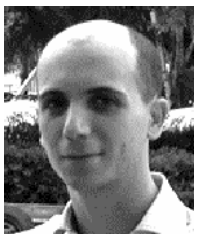

Giuseppe Genchi graduated in mechanical engineering at University of Palermo (Italy) in 2009. Currently he is a Ph.D. student in Mechanical Engineering, in the field of fluid machines, at the University of Palermo. His main research activity is the simultaneous combustion of gaseous fuel and gasoline mixtures in spark ignition engines, with particular regards to the octane rating and supercharged engine application of the natural gas-gasoline and LPG-gasoline mixtures.

Emiliano Pipitone graduated in Mechanical Engineering in 1999 at the University of Palermo, where he has been an assistant professor in the field of Fluid Machine since March 2001. He is currently lecturer in "Machine" and in "Internal Combustion Engine" and head of the internal combustion engine laboratories of the Department. He carried out experimental and theoretical researches on internal combustion engine fuel injectors, combustion diagnosis and optimal phase control, detection and measurement of knocking phenomena, fluid dynamics of engine intake systems, engine modeling and use of gaseous fuels for spark ignition engines.